



# New experimental method for the simultaneous determination of concentration and size profiles of condensed combustion products around a burning aluminum droplet

Hugo Keck, Christian Chauveau, Guillaume Legros, Stany Gallier, Fabien Halter

## ► To cite this version:

Hugo Keck, Christian Chauveau, Guillaume Legros, Stany Gallier, Fabien Halter. New experimental method for the simultaneous determination of concentration and size profiles of condensed combustion products around a burning aluminum droplet. *Combustion and Flame*, 2024, 268, pp.113616. 10.1016/j.combustflame.2024.113616 . hal-04666690

**HAL Id: hal-04666690**

**<https://cnrs.hal.science/hal-04666690v1>**

Submitted on 2 Aug 2024

**HAL** is a multi-disciplinary open access archive for the deposit and dissemination of scientific research documents, whether they are published or not. The documents may come from teaching and research institutions in France or abroad, or from public or private research centers.

L'archive ouverte pluridisciplinaire **HAL**, est destinée au dépôt et à la diffusion de documents scientifiques de niveau recherche, publiés ou non, émanant des établissements d'enseignement et de recherche français ou étrangers, des laboratoires publics ou privés.



Distributed under a Creative Commons Attribution 4.0 International License



# New experimental method for the simultaneous determination of concentration and size profiles of condensed combustion products around a burning aluminum droplet

Hugo Keck<sup>a,\*</sup>, Christian Chauveau<sup>a</sup>, Guillaume Legros<sup>a,b</sup>, Stany Gallier<sup>c</sup>, Fabien Halter<sup>a,b</sup>

<sup>a</sup> ICARE-CNRS, 1C Avenue de la Recherche Scientifique, Orléans, 45100, France

<sup>b</sup> University of Orléans, Château de la Source, Orléans, 45100, France

<sup>c</sup> ArianeGroup, Le Bouchet Research Center, Vert-le-Petit, 91710, France

## ARTICLE INFO

### Keywords:

Aluminum  
Combustion  
Alumina nano-particles  
Concentration  
Size

## ABSTRACT

When an aluminum particle burns in the diffusive regime, a cloud of nanometric particles of its primary oxide, alumina, is formed around the droplet. Characterizing this oxide smoke surrounding a burning aluminum droplet is essential. The original contribution of this paper is to introduce an experimental approach that allows for simultaneous size and concentration measurement of the particles composing the oxide smoke. This paper employs an electrodynamic levitator to facilitate the self-sustained combustion of an isolated aluminum particle, with a radius of 35  $\mu\text{m}$ , in atmospheric air. This levitation apparatus is paired with an optical setup that allows for a multi-spectral light extinction method. This technique is specifically designed to measure the size and concentration of alumina particles below the micrometric scale, which is scarcely documented in existing literature. Consequently, spatially resolved concentration and size profiles of the nanometric alumina particles are measured and compared to simulated data from the literature. The radii of alumina particles in the cloud are found to evolve closely around 80 nm. Volume fractions are evaluated from  $2.8 \cdot 10^{-4}$  near the particle surface to  $3 \cdot 10^{-5}$  further in the cloud. Therefore, significant concentrations of alumina particles are revealed during the short (15 to 20 ms) combustion process at distances of the order of magnitude of a few initial particle diameters. Such characterization could then lead to a better assessment of the interaction distance among aluminum particles as they burn collectively.

### Novelty and significance statement

This article introduces the first experimentally determined profiles of alumina concentration and size distribution surrounding a single burning aluminum droplet. The uniqueness of our experimental setup lies in its ability to study of the most fundamental case of the autonomous combustion of a single levitating particle, without any convective effects. A new non-intrusive method specifically designed provides unprecedented results in the field of metallic particle combustion. Data provided in the paper are crucial as they serve as the first reference case for future simulation and experiments. The results introduced in this paper highlight the inability of current simulation methods to accurately account for nucleation and condensation processes, and emphasize the need for a non-invasive characterization method.

## 1. Introduction

The use of aluminum combustion is prevalent in space and military applications due to its ability to significantly increase the gas temperature of solid rocket motors, thereby improving performances [1,2]. Aluminum is also being increasingly considered as a new energy source due to its carbon-free combustion and its availability as a material [3]. However, despite an increasing number of studies focused on aluminum

combustion, the underlying phenomenology is complex and not yet fully comprehended.

Numerous studies [4,5] have investigated aluminum flames, resulting in a deeper knowledge of metallic flames. While aluminum particles are typically used in the form of dust in the industry, the study of an isolated aluminum particle can provide fundamental results that could enhance the understanding of metallic dust flames [6,7]. In air at atmospheric pressure, aluminum meets the Glassman criterion [8] and

\* Correspondence to: Laboratoire ICARE-CNRS, 1C Avenue de la Recherche Scientifique, 45100, Orléans, France.

E-mail address: [hugo.keck@cnrs-orleans.fr](mailto:hugo.keck@cnrs-orleans.fr) (H. Keck).

burns in a diffusive regime for sufficiently large particles [5]. In this regime, the vaporization-dissociation temperature of the oxide exceeds the boiling temperature of aluminum. Therefore, aluminum evaporates from the droplet surface to react with the oxidizing mixture, inducing a flame detached from the surface of the droplet. Upon reacting with oxygen, intermediate gaseous suboxides are formed ( $\text{AlO}$ ,  $\text{Al}_2\text{O}_2$ ,  $\text{AlO}_2$ ,  $\text{Al}_2\text{O}$ ) before forming condensed-phase  $\text{Al}_2\text{O}_3$ , the main oxide, also called alumina [7]. Complete oxidation of aluminum thus forms a smoke composed of nano-particles of alumina [9] that may either diffuse away from or back to the droplet's surface [10].

In the field of spatial propulsion, the characterization of the produced alumina is of high importance as its presence can induce two-phase performance losses upon ejection [11] and thermo-acoustic instabilities [12]. Some studies have already attempted to characterize this alumina cloud using quenching methods. However, only a few normalized concentration profiles have been experimentally obtained [13,14] while most have only been simulated [10,15–17]. The size distribution of final alumina particles has also been estimated by collecting the condensed combustion products [9,18] and subsequently used to develop size distribution models [15,17]. However, such collection is intrusive and can potentially bias the obtained size distribution.

In this work, we aim to use a non-intrusive approach based on the light extinction method initially developed for soot characterization [19–22] to characterize the alumina cloud surrounding the aluminum droplet burning in air at atmospheric pressure. Additionally, a multispectral method is introduced, that allows for the computation of a size profile for nanometric alumina particles. In situ spatially-resolved concentration and size distribution profiles are thus obtained through non-intrusive measurements.

The methodology implemented to measure spatially-resolved volume fraction profiles as well as size distribution profiles is introduced in Section 2. The experimental setup and associated diagnostics allowing the stabilization of an isolated particle are recalled in Section 3. The results obtained are then presented and discussed in Section 4, followed by a brief conclusion.

## 2. Methodology

This section presents the methods used to determine both alumina concentration profiles as well as size distribution profiles. The first subsection introduces the general light extinction method while the second subsection elaborates its multispectral application.

### 2.1. Light extinction method

The light extinction method is based on Beer–Lambert's law that correlates the optical depth of a medium to the number density of the attenuating species composing the medium. The system under consideration, as depicted in Fig. 1, is a single aluminum droplet burning in air at atmospheric pressure.

For a light ray with an initial intensity  $I_0$  and wavelength  $\lambda$  passing through the alumina smoke along an optical path of length  $l$  and with a final intensity of  $I$ , Beer–Lambert's law gives:

$$\tau(\lambda) = \int_l \tau_{loc}(z, \lambda) dz = -\ln\left(\frac{I}{I_0}\right) \quad (1)$$

With  $\tau(\lambda)$  being the optical depth of the medium integrated along the optical path, at the wavelength  $\lambda$ .  $\tau_{loc}(z, \lambda)$  is the local optical depth of the medium at the distance  $z$  from the origin of the light ray. The ratio  $\frac{I}{I_0}$  is also called the transmittance of the medium.

The optical depth of the alumina cloud is experimentally assessed using a Light-Emitting Diode (LED) as a backlight. The LED, of initial intensity  $I_0$  is positioned so that it emits along the optical path introduced in Fig. 1, and thus reaches the camera sensor with a lower intensity  $I$  due to absorption by the cloud.

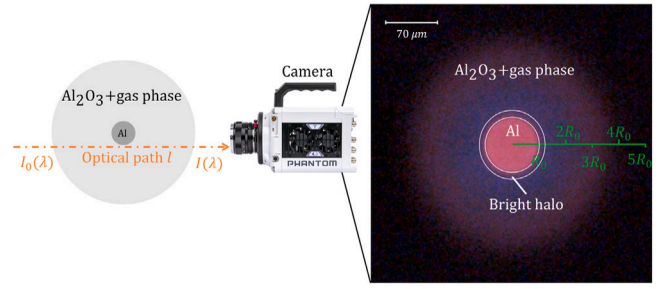


Fig. 1. The left part of the figure is a schematic of a light ray of intensity  $I_0$  passing through the oxide smoke of the burning particle along the optical path of length  $l$  and reaching the camera sensor with an intensity  $I$ . The right part of the figure is an example of image obtained for a particle burning in air at atmospheric pressure. The image is captured with a color camera and with no backlight (meaning no light ray of known initial intensity). Non-dimensional scale is added for clarity and further purpose ( $R_0 = 35 \mu\text{m}$ ). The frame is capture 1.4 ms after ignition and laser cut off. (For interpretation of the references to color in this figure legend, the reader is referred to the web version of this article.)

In the case of a non-emitting smoke, a pair of images would suffice to compute the integrated optical depth. A simple pixel by pixel division of an image of the smoke lit with a LED by an image of the LED alone would yield an image of the transmittance of the medium. However, in the case of a burning aluminum droplet, the cloud is composed of light emitting gases and nano-particles. Upon assessing the amount of light absorbed by the cloud, the increase in intensity due to flame emission itself needs to be accounted for. To do that, an additional image of the smoke, with no LED, is required and is subtracted from the image of the smoke lit by the LED. This difference cancels the cloud emission and enables the quantification of cloud absorption alone. The dark noise is also accounted for to increase the accuracy of the method.

Denoting  $I_{px}^{1,on}$  as the intensity of the pixels of the image with the particle and the LED on,  $I_{px}^{1,off}$  the intensity of the pixels of the image with the particle and the LED off,  $I_{px}^{0,on}$  the intensity of the pixels of the image with the LED alone and  $I_{px}^{0,off}$  the intensity of pixels of the dark noise image, the integrated optical depth of each pixel is computed accordingly:

$$\tau_{px} = -\ln\left(\frac{I_{px}^{1,on} - I_{px}^{1,off}}{I_{px}^{0,on} - I_{px}^{0,off}}\right) \quad (2)$$

These four images containing the required pixel intensities are obtained as illustrated in Fig. 2 and the three transmittance ratios  $\frac{I_{px}^{1,on} - I_{px}^{1,off}}{I_{px}^{0,on} - I_{px}^{0,off}}$  computed at the three wavelengths of interest from these images are presented in Fig. 3. It can be observed from Fig. 3 that a relatively good absorbance of the LED is observed and that absorbance can be assessed until about 12 to 13 droplet radii. For distances further away from the droplet, the transmittance ratio is found equal to 1. Note that all the captured images contain information integrated along the optical path. A deconvolution process is required to retrieve local information inside the cloud.

An alternate expression of Beer–Lambert's law introduces a dependence of the optical depth to the concentration of light-absorbing species accordingly:

$$\tau(\lambda) = \int_0^l \sum_i \sigma_i(z, \lambda) \cdot n_i(z) dz \quad (3)$$

The optical depth is thus the sum, for each attenuating species of the medium  $i$ , of the integrated product of their local attenuation cross section  $\sigma$  at the point  $z$  of the optical path and wavelength  $\lambda$  with their local number density  $n$ , along the optical path. Assuming that gases are optically thin, the only attenuating species considered is condensed

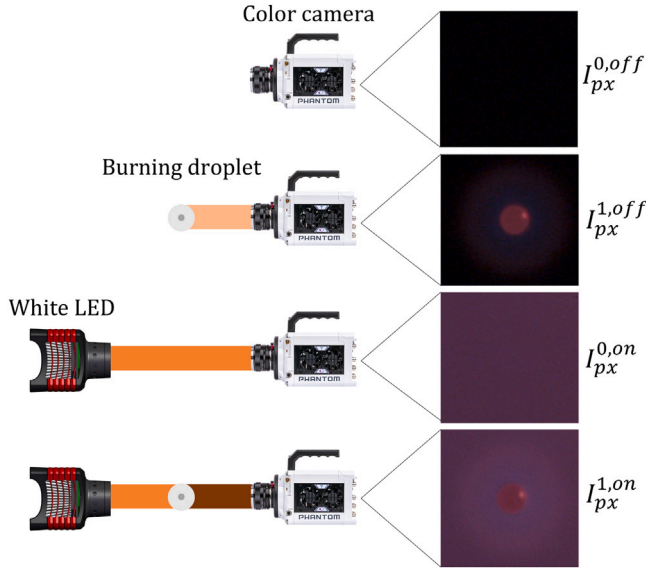


Fig. 2. Schematic of the four intensities required to calculate the integrated optical depth of the alumina cloud. Corresponding camera images obtained for an aluminum droplet of radius  $R_0 = 35 \mu\text{m}$  burning in air are also displayed.

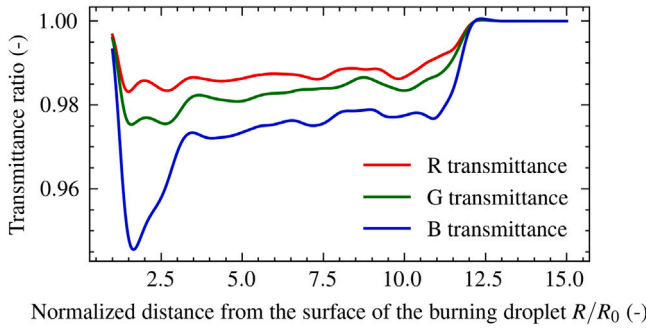


Fig. 3. Transmittance ratio profiles  $\frac{I_{px}^{1,on} - I_{px}^{1,off}}{I_{px}^{0,on} - I_{px}^{0,off}}$  for the three wavelengths of interest.

alumina. Considering alumina exists as spherical particles of radius  $r(z)$  at the point  $z$  of the optical path, Eq. (3) can be rearranged to write:

$$\tau(\lambda) = \int_0^l \sigma(r(z), \lambda) \frac{f_v(z)}{4/3 \cdot \pi \cdot r(z)^3} dz \quad (4)$$

With  $\sigma(r(z), \lambda)$  the attenuating cross section of an alumina particle of radius  $r(z)$  at a wavelength  $\lambda$  and  $f_v(z)$  the volume fraction of alumina at the point  $z$  of the optical path. The attenuation cross section for a particle of alumina can be computed using the Mie theory when the radius of the particle is known. More precisely, the attenuation cross section is computed as [23]:

$$\sigma(r(z), \lambda) = \frac{\lambda^2}{2\pi^2} \cdot \sum_{p=1}^{\infty} (2p+1) \Re(a_p(m, x) + b_p(m, x)) \quad (5)$$

where  $x$  is called the size factor of the particle computed as  $x = \frac{2 \cdot \pi \cdot r(z)}{\lambda}$ . The scattering factors  $a_p$  and  $b_p$  are composed of Riccati-Bessel functions of the size factor and of the refractive index of alumina. While detailed calculations are not shown in this work, the reader is invited to read [23] for the full derivation. It is, however, to be noted that the refractive index of liquid alumina  $m$  is taken from Dombrovsky's work [24] and is thus expressed as:

$$m(\lambda, T) = n_0(\lambda) [1 + \xi_1 (T - T_1)] + ik_0(\lambda) e^{\xi_2 (T - T_*)} \quad (6)$$

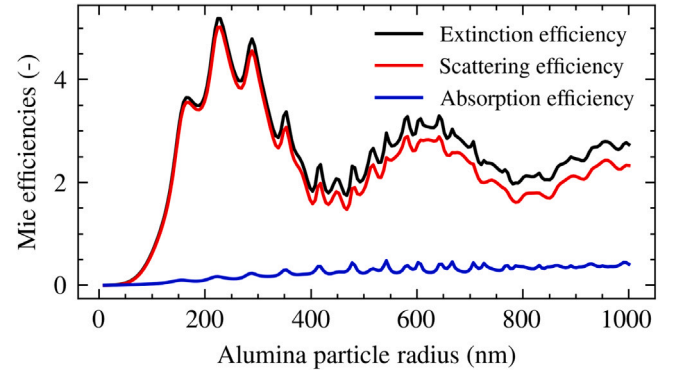


Fig. 4. Mie efficiencies for an alumina sphere of varying radius computed at a wavelength of 630 nm at a temperature of 3550 K.

With

$$n_0(\lambda) = \sqrt{1 + \frac{1.024\lambda^2}{\lambda^2 - 0.003776} + \frac{1.058\lambda^2}{\lambda^2 - 0.01225} + \frac{5.281\lambda^2}{\lambda^2 - 321.4}} \quad (7)$$

and

$$k_0(\lambda) = 0.002 \cdot (1 + 0.7\lambda + 0.06\lambda^2) \quad (8)$$

The values of the parameters are  $T_1 = 473 \text{ K}$ ,  $\xi_1 = 2.02 \cdot 10^{-5} \text{ K}^{-1}$ ,  $\xi_2 = 1.847 \cdot 10^{-3} \text{ K}^{-1}$  and  $T_* = 2950 \text{ K}$ . The wavelength for both  $k_0$  and  $n_0$  is expressed in microns. As a reference, Fig. 4 presents the Mie efficiencies (cross section divided by the projected area of the sphere) for an alumina sphere of varying radius computed at a wavelength of 630 nm. Although calculations were also performed for two other wavelengths, these results are not shown to maintain simplicity. The efficiencies at the three wavelengths of interest show minimal variations, as only the size factor  $x$  and the refractive index undergo slight changes. Temperature dependence of the attenuation cross section is negligible and thus temperature will be considered at  $T = 3550 \text{ K}$  at all points in the cloud, this temperature being the measured average temperature of the gaseous phase [25]. This can be refined with a more precise knowledge of the temperature field surrounding the particle. Fig. 5 depicts a simulated temperature profile surrounding a burning aluminum droplet under conditions similar to the experimental ones (details of the simulations are omitted here but can be found in [10]<sup>1</sup>). From this temperature profile, temperatures within the cloud are expected to range between about 2700 K (the surface temperature of the aluminum droplet) and 3750 K. To assess the influence of the temperature considered on the method, calculations have also been carried out considering cloud temperatures of 3750 K, 2700 K and 3550 K. Relative errors between the 3550 K assumption and the 3750 K assumption are of about 3% for the size profile and 13% for the volume fraction profile. Relative errors between the 3550 K assumption and the 2700 K assumption are also of about 3% for the size profile and 13% for the volume fraction profile. Given the temperature profile from Fig. 5, assuming a constant temperature of 2700 K within the oxide cloud is not a valid assumption. It is assumed that within the typical temperature range for an aluminum particle burning in atmospheric air, the considered temperature does not have a substantial effect.

Going back to Eq. (4), looking at a local point of the oxide smoke, the local optical depth  $\tau_{loc}$  at the point  $z$  of the optical path is expressed as:

$$\tau_{loc}(z, \lambda) = \sigma(r(z), \lambda) \frac{f_v(z)}{4/3 \cdot \pi \cdot r(z)^3} \quad (9)$$

<sup>1</sup> Basically, Navier-Stokes equations are solved around a burning droplet with an aluminum kinetic mechanism.



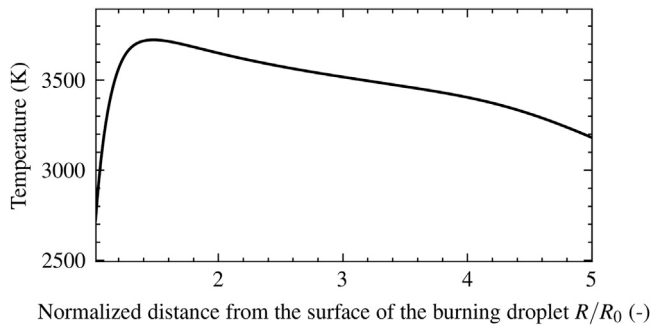


Fig. 5. Simulated temperature profile around an aluminum droplet of radius  $R_0 = 35 \mu\text{m}$  burning in 80%N<sub>2</sub>/20%O<sub>2</sub> (vol.) mixture at  $p = 1$  bar.

The local optical depth can be experimentally determined by deconvolution of the image resulting from the computation of the integrated optical depth with Eq. (2). This process uses an onion peeling method in conjunction with a Tikhonov regularization to minimize deconvolution noise. The reader is invited to consult [20] for more details about the deconvolution method. This process results in an image of the local optical depth which can be used in Eq. (9) to assess the local volume fraction of alumina. A deconvolution procedure requires a cylindrical symmetry of the processed image. Data presented in this work is extracted from phases of symmetric combustion as illustrated in Fig. 1 and a cylindrical symmetry is considered for each line of this image. An asymmetric combustion phase can occur during the combustion of an aluminum particle, primarily due to the existence of an oxide cap on the burning droplet's surface. The application of a deconvolution process during this asymmetric combustion phase is intricate. A significant amount of alumina is usually transferred between the oxide cap and the oxide cloud during this phase, generating a cone of high concentration [10]. To study such phenomena using the proposed methodology, it is necessary to capture images where the symmetry axis of the high-concentration cone aligns with the camera sensor's plane. Capturing such images is highly complex, as jetting and spinning of the droplet are frequent outcomes of the asymmetric burning phase. To summarize, a deconvolution operator  $dec$  is introduced such as  $dec(\tau)$  yields the local value of  $\tau$ . We then write:

$$dec(\tau_{px}) = \frac{\sigma(r(z), \lambda) \cdot f_v(z)}{4/3 \cdot \pi \cdot r(z)^3} \quad (10)$$

The procedure of onion peeling is an Abel transform that enables the retrieval of local information. In the context of this work, any value that is introduced is considered a local value. The values that are convoluted (or integrated) are not the focus of this study.

Eq. (10) is dependent on the size of alumina particles that yet needs to be assessed. Theoretically, for particles significantly smaller than the considered wavelength, the Rayleigh approximation can be applied eliminating the dependence of the optical depth on the particle radius since  $\sigma \propto r^3$ . Calculations revealed that this approximation introduces significant computational errors for alumina particles with radii larger than 10 nm and LED emission in the visible spectrum. Fig. 6 illustrates an arbitrary volume fraction evaluation assuming an arbitrary local optical depth of 0.03. The volume fraction computed using the Rayleigh approximation is indeed independent of the particle size considered. In contrast, the volume fraction calculated without the approximation is dependent on the considered radius and highly significant differences between the two curves are observed for radii above a few nanometers. An error of 100% is already noted for a particle radius of 20 nm while most of the literature predicts alumina nano-particles to have a radius of a few hundred nanometers [14,15]. Therefore, for greater accuracy, this approximation is not used and a multispectral method presented in the next subsection is implemented to determine the local size of alumina nanoparticles.

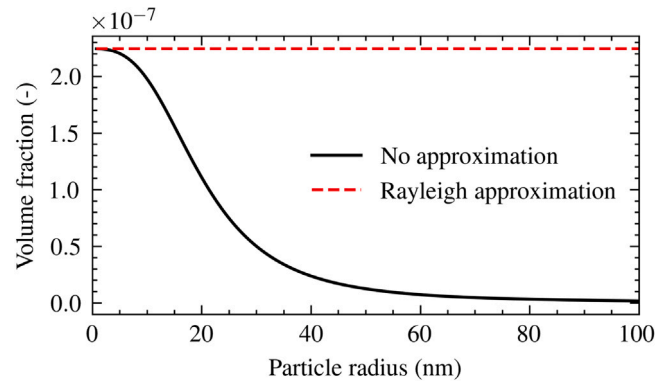


Fig. 6. Volume fraction computed from an arbitrary local optical depth  $\tau_{loc} = 0.03 \text{ m}^{-1}$  local optical depth at a wavelength of 455 nm as a function of the considered particle radius. Rayleigh approximation fails for alumina size above a few nanometers.

## 2.2. Multispectral light extinction method

The multi-spectral application of the light extinction method consists in a simultaneous measurement of a medium's optical depth at various wavelengths. The volume fraction of alumina as well as the particle radius are independent of the wavelength at which they are measured. Thus,  $\frac{f_v(z)}{4/3 \cdot \pi \cdot r(z)^3}$  remains constant regardless of the wavelength considered. Hence, reworking Eq. (9),  $\tau_{loc}(z, \lambda)/\sigma(r(z), \lambda)$  is also constant when  $z$  is fixed. Consequently, for two different wavelengths  $\lambda_1$  and  $\lambda_2$ , we can write:

$$\frac{\tau_{loc}(z, \lambda_1)}{\sigma(r(z), \lambda_1)} = \frac{\tau_{loc}(z, \lambda_2)}{\sigma(r(z), \lambda_2)} \quad (11)$$

By simultaneously measuring the optical depth  $\tau_{loc}$  at different wavelengths, the only variable that remains unknown is the local attenuation cross section  $\sigma(r(z), \lambda)$ . This variable can be calculated as a function of the particle radius using Mie theory. An optimization procedure is carried out to determine the particle size profile within the oxide smoke cloud that solves Eq. (11) for each pair of wavelength ((450 nm, 530 nm), (450 nm, 630 nm) and (530 nm, 630 nm)). The optimization procedure is based on minimizing the relative error between the values of the three ratios  $\frac{\tau_{loc}}{\sigma}$ . Errors based on experiments are not evaluated for extinction cross sections since they are inferred from Mie theory. Nonetheless, the local optical depth is affected by an experimental error as it is calculated from a ratio of pixel intensities. Pixel values present a fluctuation of about 1% around their mean value, resulting in an error of about 8% on the optical depth values. This pixel value fluctuation has no impact over the assessment of the size of nanometric alumina particles. Indeed, the optimization process is applied to each pixel and the fluctuation in pixel value is consistent across the three RGB channels of the involved pixel. Consequently, if the optical value for a specific pixel has an 8% error, this error is identical for the R, G, and B channels and therefore nullifies when applied to Eq. (11), resulting in a 0% error on the subsequent size profile. A sensitivity analysis of the optimization process would be valuable in the case of a spectral error when computing the optical depths. A spectral error can arise if spectral overlap is not taken into account, thereby making the ratio of optical thickness for two different wavelengths incorrect. However, a calibration procedure is executed to compute spectral overlap and the spectral error between optical depths at two different wavelengths is negligible. A study has nonetheless been carried out for one combustion case, varying simultaneously the three optical thicknesses by a random percentage ranging from minus 5% to 5%. This has been done 20 times and the size profiles resulting from the optimization procedure differ by a mean relative error 2.5% from the initial profile and a mean absolute error of 1.9 nm from the initial profile. Note, however,

that the 8% error on the optical thickness does apply linearly to the evaluation of the volume fraction computed after the assessment of the size of nanometric alumina particles. Once the size distribution has been determined, it can be applied to Eq. (10) to obtain a volume fraction measurement without using the Rayleigh approximation. It is important to note that for the method to be applicable, the light extinction from the oxide cloud must be assessed and extinction cross sections must be calculated. The Mie theory has no upper size limit as solutions converge towards geometric optics solutions for larger particles sizes and thus no size limitations are known for the computation of extinction cross sections. Limitations, however, exist for the light extinction measurements. Low concentrations lead to non-measurable absorbances while high concentrations can lead to an optically thick medium, both of which hinder light extinction evaluations. Numerical values for volume fraction limits are not known but are expected to be assessed in future experiments. The experimental setup and diagnostics that allow for such measurements are presented in the next section.

### 3. Experimental setup and diagnostics

This section provides an overview of the experimental setup and the diagnostics used. The first subsection introduces the levitating and ignition devices, while optical diagnostics are introduced in Section 3.2.

#### 3.1. Electrodynamic levitator and laser ignition

The electrodynamic levitator, depicted in Fig. 7, is used to achieve combustion of a single isolated aluminum particle with minimal external interactions. Aluminum particles, of approximately  $35\ \mu\text{m}$  in radius, are charged via friction in a syringe and then introduced in the levitator through the injection port. The DC supplied electrodes enable compensation of the weight of the particle while the AC supplied circular electrode creates an equilibrium location for the particle at the device's center by generating an alternating electric potential. Four optical ports localized on the circular electrode enable laser ignition as well as access for the optical diagnostics introduced in the next subsection. A 50 W  $\text{CO}_2$  laser is split into two identical beams directed into two opposite optical accesses of the levitator, impacting the particle from both sides. This enables a symmetric heating of the particle and minimizes particle displacement due to radiative pressure effects. The ignition system is coupled to a photomultiplier that shuts off the laser when sufficient luminance is detected through one of the other optical accesses so that thermal runaway can occur and self-sustained combustion can be observed. Once the particle is ignited, optical diagnostics introduced in the following subsection allow for the measurement of the previously mentioned profiles.

#### 3.2. Optical diagnostics

As previously noted, a light extinction method is employed to evaluate alumina size distribution profiles and volume fraction profiles. This requires the optical depth to be measured simultaneously for different wavelengths. A white LED SOLIS-3C serves as a backlight, illuminating the burning particle while a high-speed color camera PHANTOM T-2410 paired with a triple band filter (450 nm, 530 nm, 630 nm) and a QUESTAR QM 100 teleobjective measures light intensity at three different wavelengths using the camera's RGB matrices. Flame emission must be subtracted from the image of the illuminated particle to measure light absorbed by the oxide smoke. Therefore, the LED is pulsed at half the frequency of the camera, enabling the use of two successive images with minimal spatial variation of the system between the two images. The camera operates at a frequency ranging from 4 kHz to 18 kHz leading to a maximum delay between successive frames of 0.25 ms for usual combustion times ranging from 15 to 20 ms. RGB matrices of the camera coupled with the triple band filter are considered respectively as 630 nm, 530 nm and 450 nm images. Note

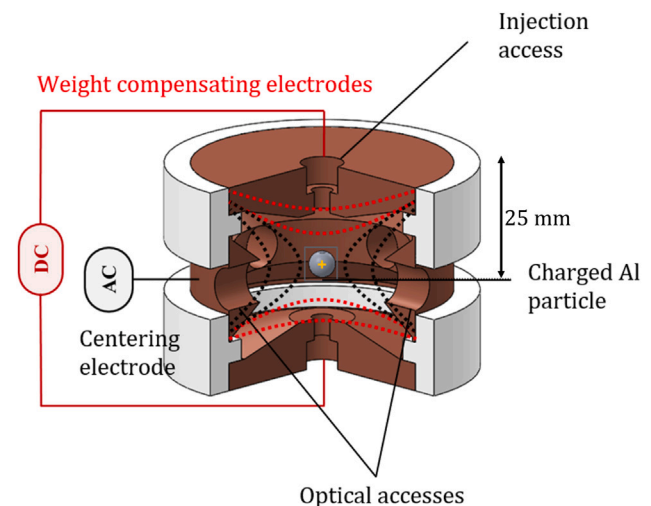


Fig. 7. Schematic of the electrodynamic levitator. For clarity, the particle is depicted larger than its actual size.

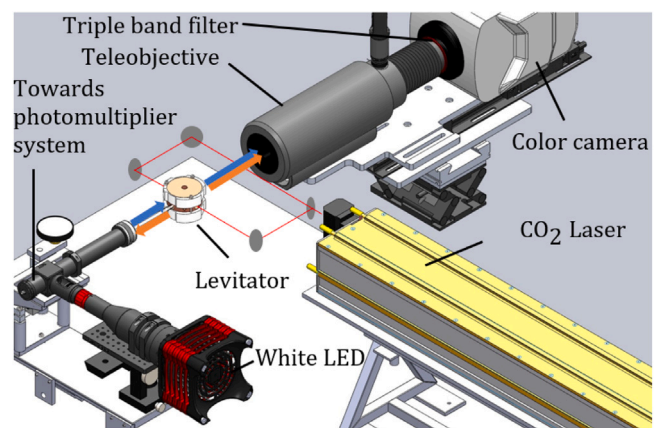


Fig. 8. Schematic of the full experimental setup, including the pathways of the  $\text{CO}_2$  laser beam (red line), the LED light (blue arrows), and the combustion emissions (orange arrows). (For interpretation of the references to color in this figure legend, the reader is referred to the web version of this article.)

that a calibration has been carried out using simple band filters at the same wavelengths as the triple band filter in order to determine the spectral overlap of the camera. This method is similar to the one used in Ref. [26]. Metal particle combustion is a highly luminous process and camera sensors may saturate upon recording. The use of high speed cameras such as aforementioned allows for minimum exposure times of very low values, giving the possibility to comfortably modulate the amount of light impinging the camera sensor. Reducing the exposure time also benefits the time resolution of the data as the frequency of the camera can be increased. However in this study, the triple band filter significantly reduces the amount of light reaching the camera sensor. The filter's presence necessitates a longer exposure time and a lower camera acquisition frequency, leading to the use of the stated frequencies instead of the camera's maximum acquisition frequency of 78 kHz. This limitation negatively impacts the time resolution of the acquired data. This is not crucial in this study as the temporal evolution of the introduced size and volume fraction profiles are not discussed and the current frequency already allows for a minimal displacement of the droplet between two successive frames allowing for the use of the light extinction method. The global experimental setup is illustrated by Fig. 8.

## 4. Results and discussion

This section introduces results obtained for 35  $\mu\text{m}$  average radius aluminum particles burning in air at atmospheric pressure. The first subsection focuses on the size distribution profile of alumina particles, while the second subsection presents the volume fraction profiles obtained based on the results from Section 4.1.

### 4.1. Size distribution profile

Firstly, local optical thickness profiles are derived from deconvolution of the negative natural logarithm of the transmittance image (Eq. (1)). As a reminder, the transmittance image is obtained by subtracting the flame emission from an image of an illuminated flame and then dividing it by the LED emission alone (Eq. (2)). The local optical depth images obtained are shown in Fig. 9 on a logarithmic scale for the three wavelengths of interest. This figure emphasizes the discrepancies in local optical thickness values depending on the wavelength considered for evaluation. Given that optical thickness is proportional to emissivity, the dependence of this factor with the wavelength is underscored. This points out that the grey body assumption may not be suitable for calculating local temperatures in the cloud in future studies. Indeed, the grey body hypothesis assumes that the three optical depths are equal. Also, the significant differences between the three images of Fig. 9 advocate for the use of a multispectral method for size measurements as the optimization process described earlier has the potential to substantially reduce the discrepancies among the three  $\tau_{\text{loc}}/\sigma$  ratios. Images in Fig. 9 are averaged images. An averaged absorbance profile is computed so that a value of this profile at a distance  $x$  from the center of the droplet is the average of the optical thicknesses of all pixels located at a distance  $x$  from the center of the droplet. This averaged profile is then reconstructed as a 2D image surrounding the droplet yielding images from Fig. 9.

Once the optical depth profiles are obtained, an optimization procedure is performed for each point of the profile to find an alumina particle radius  $r(z)$  that satisfies Eq. (11) for the three wavelength pairs for which the optical depth was measured. As a result of this optimization, a size distribution profile is obtained for the case of 35- $\mu\text{m}$ -radius aluminum particles burning in air at atmospheric pressure. The resulting profile has been averaged for about 6 different cases of aluminum particle combustion. For each case, about 5 different instants of the combustion are studied, resulting in a total of 30 experimental points. In the six cases examined, combustion times vary between 15 ms and 17 ms. The times for the selected combustion instants range between 2.4 ms and 6.5 ms after ignition, corresponding to 15% to 32% of the corresponding combustion times. During these instants, the droplet burns in a symmetric regime. It should be noted that the size determined considers that nano-particles are spherical. Therefore, the radii presented in this section should be viewed as characteristic alumina sizes rather than sphere radii, as no information about the geometry of the condensed combustion products can be obtained. It is important to note that large agglomerates of alumina can optically behave like smaller alumina spheres and vice versa due to potential peculiarities of their geometry. Nevertheless, the melting temperature of alumina is of approximately 2300 K and temperatures within the oxide smoke cloud are expected to be significantly higher than 3000 K as illustrated by Fig. 5. Therefore, alumina particles are therefore liquid in the vicinity of the aluminum droplet. Upon considering liquid alumina particles, a spherical geometry must be considered. Moreover, within the aforementioned temperature range, alumina droplets undergo nucleation, growth and possibly coalescence, the latter inducing only slight changes in droplet size. The formation of aggregates such as those observed by Glotov et al. [27] are expected to occur only in the event of solid alumina particles. The existence of agglomerates within the cloud is physically unexpected, and thus the measured sizes are assumed to be local average sizes of single alumina particles. The size

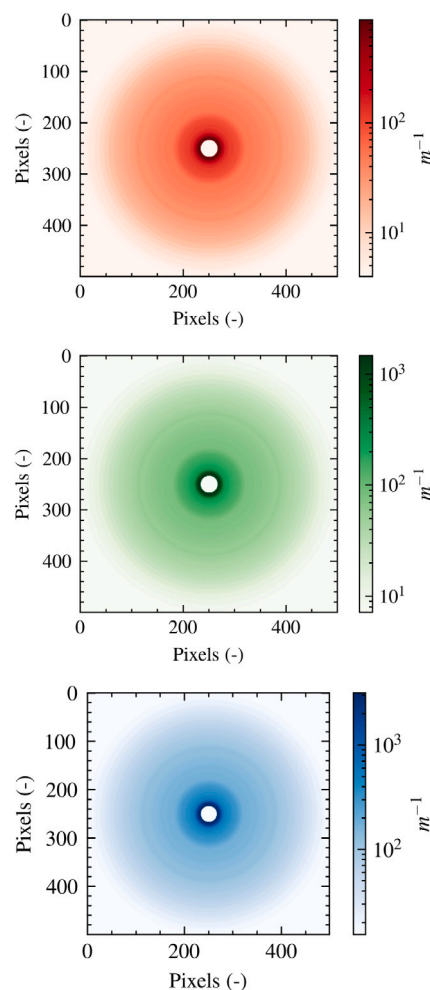


Fig. 9. Colormaps of the Red (630 nm), Green (530 nm) and Blue (450 nm) local optical depth images obtained by deconvolution of the opposite of the logarithm of the transmittance images. The droplet is represented by the white circle at the center of the image. Optical depths are displayed according to a logarithmic scale for the sake of clarity. (For interpretation of the references to color in this figure legend, the reader is referred to the web version of this article.)

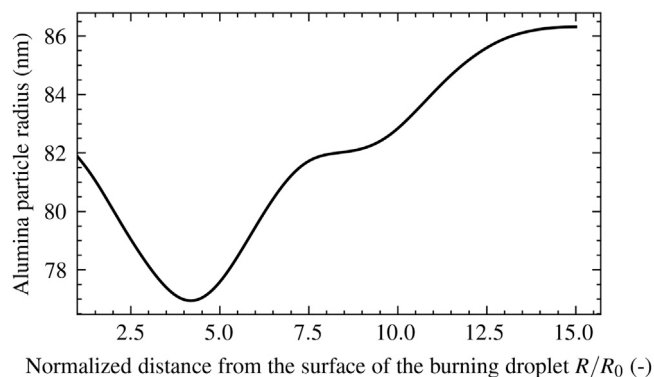


Fig. 10. Alumina size profile around an aluminum droplet of radius  $R_0 = 35 \mu\text{m}$  burning in atmospheric air.

profile for alumina nano particles is shown in Fig. 10. The efficiency of the optimization is discussed in the next subsection as it relates to volume fraction profiles.

The resulting size profile present sizes of alumina nanometric particles varying closely around the mean value of the profile of 81 nm.



Variations of sizes within this profile are significantly low and of less than 4 nm. The physical interpretations of the size variations presented in this section are thus purely theoretical and definitive conclusions cannot be drawn as size variations are too low and are believed to lie below the precision threshold of the method. At the surface of the particle, a radius of about 82 nm is measured. The size then decreases monotonously until 4 droplet radii reaching a radius of 75 nm. For greater distances to the droplet surface, the alumina particle radius increases until about 15 droplet radii reaching a radius value of about 86 nm. The region located between 3 to 5 droplet radii containing the minima of the profile is considered as the reaction zone, where most oxidizing reactions happen and where the temperature peak would be located. At this location, a mainly red region can be observed in Fig. 1 due to high temperatures of condensed phase alumina. The temperature of the gaseous phase in the cloud has been experimentally evaluated at about 3550 K using a spectrometry method [25]. This temperature is considered the highest in the system, making condensation and coalescence phenomena less favored than in colder regions of the cloud. Particles located in the reaction zone are likely recently formed and thus less time has been allocated for coalescence to occur. As a result, particles are generally smaller in this hot region of the cloud.

Close to the droplet, for  $R/R_0 < 3$ , a significant temperature gradient exists between the droplet temperature presumably around the boiling temperature of aluminum, and the gas phase temperature. Particles located at radii lower than 3 particle radii experience a sharp temperature drop. Moreover, due to the spherical geometry of the system, particles located between 1.5 and 2 particle radii are located in a smaller volume than particles located between 3.5 and 4 particle radii for instance. Therefore, particles diffusing closer to the droplet are located in a reduced volume, leading to particles being closer together. This proximity and temperature gradient favor the condensation and coalescence phenomena, inducing larger nano-particles of alumina. A similar trend is observed on the other side of the reaction zone for radii greater than 5 particle radii where another temperature gradient exists due to thermal losses to the atmosphere and to boundary conditions with the surrounding environment at a temperature of 300 K. Consequently, the increase in particle radius moving from 3 to 1 droplet radii and from 5 to 15 droplet radii is most likely due to alumina coalescence and condensation.

It is to be noted that size profiles and concentration profiles are closely related. The presence of larger particles close to the surface of the particle can also be explained by a local increase in the concentration as it can be observed in the next subsection. Volume fraction profiles are also impacted by particle sizes as heat release from condensation, volume heat losses from particles or particle diffusion are processes that can impact the general motion of particles and thus the location of high concentration regions.

There is very limited data referenced for the conditions of the experiments presented here (and none reported in a non-intrusive way). To our knowledge, there are no documented sizes of nanometric alumina for the scenario of an isolated burning droplet in existing literature. However, some studies have reported sizes of nanometric alumina particles determined from samples collected post-combustion. Ref. [28] showcases TEM images of nanometric alumina particles recovered from an Al/Air flame. The nanometric products exhibit a size distribution with a mode at a radius of 65 nm, which is about 10 nm less than the size of the smallest radius presented in this study. Similarly, Glotov et al. [27] recovered clusters of nanometric alumina particles generated by the combustion of an aluminized propellant, and found that the spherical radii do not surpass 75 nm. Acceptable discrepancies are observed between the results introduced in this work and sizes assessed from combustion products. Results however are roughly comprised between 65 and 85 nm leading to a relatively good estimation of alumina nanometric particle size. It is, however, to be noted that the burning conditions of the two previously mentioned references are significantly different from the burning conditions of a single aluminum

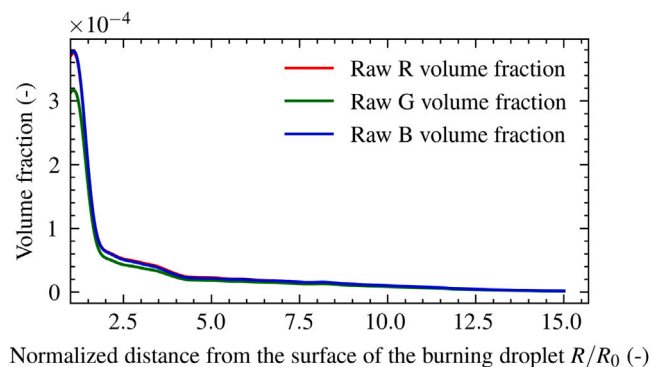


Fig. 11. Non-optimized alumina volume fraction profiles around an aluminum droplet of radius  $R_0 = 35 \mu\text{m}$  burning in air assuming a 75 nm alumina particle radius.

droplet. Aluminum particles burning collectively are impacted by external heat sources such as other burning droplets. The existence of these external heat sources alters the combustion phenomenology and the temperature of the gases surrounding the burning droplet. In the case of this work, the atmosphere is at room temperature while aluminum droplets burning in a flame are located in a hot atmosphere. Lastly, both of the cited references depict aluminum droplets burning within a flow (either due to gravity or forced flow), while the isolated droplet in this study burns with minimal displacement. It is believed that variations in the burning process might affect phenomena such as the cooling of nanometric alumina particles. This is thought to possibly alter the size of nanometric combustion products, and sizes determined from collective combustion products might not be directly comparable to in situ measurements for an isolated burning droplet.

Once the size profile of alumina has been determined, the volume fraction of alumina can be computed. Results are presented in the following subsection.

#### 4.2. Volume fraction profile

Having determined the size profile, Eq. (10) can be inverted and used to determine a volume fraction profile for a known alumina size. Prior to applying the multispectral light extinction method and its optimization process, non-optimized volume fraction profiles can be computed using Eq. (10), assuming a constant alumina particle radius of 75 nm throughout the cloud. The results, shown in Fig. 11 reveal significant discrepancies between the three profiles, indicating the need for an optimized alumina particle size profile.

By applying the multispectral method and its associated optimization process, the alumina size profile shown in Fig. 10 can be used to compute more accurate volume fraction profiles. These optimized profiles, shown in Fig. 12, have an average relative error of  $3.5 \cdot 10^{-14}$  % to the average profile calculated as a third of the sum of the R, G and B profiles, compared to the 7.2% error of the non-optimized profiles in Fig. 11. This decrease in discrepancies indicates that the optimization process was successful, as the alignment of the three-volume fraction profiles is a direct result of correctly optimizing the alumina size for Eq. (11).

Since these three profiles are similar, the total alumina volume fraction profile is taken as the average of the optimized R, G and B volume fraction profiles. The alumina volume fraction profile calculated for a 35- $\mu\text{m}$ -radius aluminum particle burning in air at atmospheric pressure is shown in Fig. 13.

A peak of alumina concentration is measured at the particle surface and reaches a value of  $2.8 \cdot 10^{-4}$ . Further away from the surface, alumina concentration sharply decreases to reach a value of  $4.1 \cdot 10^{-5}$  at 2.5 droplet radii. From 2.5 to 3.5 particle radii, the volume fraction of alumina remains fairly constant with only a slight decrease in



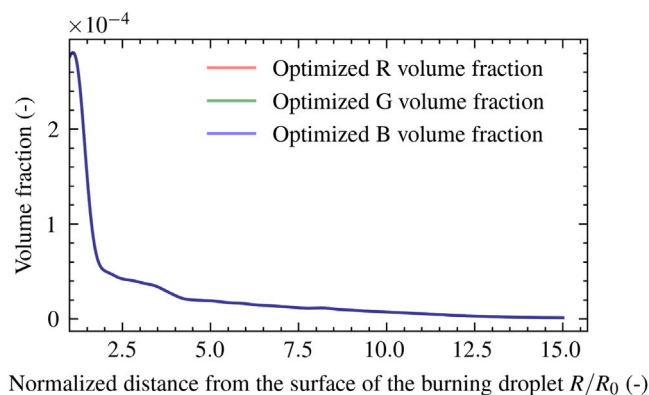


Fig. 12. Optimized alumina volume fraction profiles around an aluminum droplet of radius  $R_0 = 35 \mu\text{m}$  burning in air.

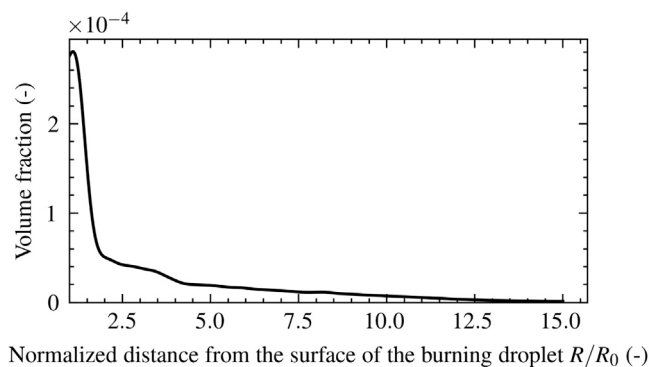


Fig. 13. Alumina volume fraction profile around an aluminum droplet of radius  $R_0 = 35 \mu\text{m}$  burning in air.

concentration. Even further away, for distances ranging from 3.5 to 13 droplet radii, alumina concentration decreases monotonously and reaches negligible values after 12 to 13 droplet radii, aligning with the transmittance ratios presented in Fig. 3.

Ignoring at first the high concentration of alumina at the surface of the droplet, the plateau of volume fraction observed at about 2.5 particle radii acts as a local maxima of the concentration profile. This fairly high concentration in alumina corresponds in Fig. 1 to the edge of the red halo on the image indicating emission from a region of high concentration of condensed phase. Even though this local high concentration in alumina is observed by both Bucher [14] and Dreizin [13], it is wrongly located in most of the simulated profiles as it can be seen in Beckstead's data [29], see Fig. 15 for example.

Particles formed in the reaction zone diffuse away towards the droplet or towards the fresh gases, increasing in size. Phoretic motions driven by temperature and concentration gradients induce back-diffusion of the formed oxides towards the surface of the particles [10]. Particles diffusing close to the droplet are located in a smaller volume due to the spherical geometry of the system, resulting in a greater volume fraction, as depicted in Fig. 13. It is also to be noted that in addition of particle diffusion towards the droplet, formation of nanoparticles of alumina can also happen close to the aluminum droplet. Indeed, simulations indicate that species required for alumina production are available close to the droplet, outside of the main reaction zone suggested earlier. Fig. 14 shows simulated concentrations of gaseous species at the surface of a burning aluminum droplet in similar conditions as the experimental ones (simulation details are skipped here and

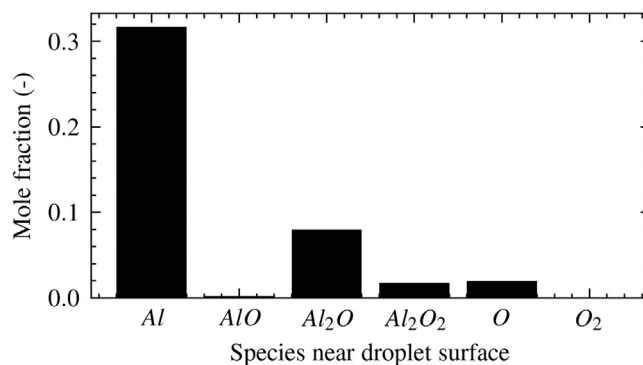


Fig. 14. Simulated concentrations of gaseous species at the surface of an aluminum droplet of radius  $R_0 = 35 \mu\text{m}$  burning in 80% $\text{N}_2$ /20% $\text{O}_2$  (vol.) mixture.

can be found in [10]<sup>2</sup>). For clarity,  $\text{N}_2$  is not displayed here but is the main species at the surface with a mole fraction of about 0.56. Non-negligible concentrations of  $\text{Al}_2\text{O}$ ,  $\text{Al}$ ,  $\text{AlO}$  and  $\text{O}$  are computed at the droplet surface, suggesting possible alumina formation in this region due to classic vapor phase reaction or surface reactions. However, no definitive conclusions can be drawn yet concerning the origin of the particles in this region as neither back-diffusion nor local production phenomena are characterized here. Referring back at Fig. 1, the volume fraction measured close to the droplet surface matches the presence of a bright reddish halo observed at the edge of the droplet by the camera, indicating a high concentration of condensed emitting species. Such a phenomenon was not predicted by simulations, neither from Beckstead [29] nor from Bucher [14]. This particular phenomenon is highlighted in this work and is observed, less prominently, in Dreizin's experimental data as a non-negligible oxide concentration close to the droplet [13] is shown. Bucher's experimental setup [14] however did not allow for near-droplet volume fraction evaluation.

Finally, the measured volume fraction assessed for distances greater than 8 particle radii aligns relatively correctly with results from present simulations as observed in Fig. 15. Present simulation details can be found in [10]. Significant discrepancies are however observed for any distance to the surface lower than 8 droplet radii. The explanations for these discrepancies are yet to be studied. However, the way condensation processes are accounted for in the simulations might be of particular interest. Particle nucleation, coalescence or heat release are complex phenomena and an inaccurate modeling could result in an imprecise accounting for oxide diffusion processes. The impact of oxide diffusion processes on concentration profiles is currently being studied. To compare the obtained experimental results to simulated mass fraction profiles found in the literature, assumptions have to be made regarding unknown parameters. Upon using a mean gas density in the cloud of  $0.12 \text{ kg/m}^3$  and a mean alumina density of  $2300 \text{ kg/m}^3$ , an experimental mass fraction profile can be computed and compared to simulated mass profiles in Fig. 15. This figure summarizes all the discrepancies mentioned earlier between experimental and simulated data including profiles lengths, peak locations as well as near-droplet phenomena.

With the knowledge of the volume fraction profile and in the aim of providing more data for simulation purposes, the mass of the oxide cloud can be computed by integrating the profile over the whole volume and multiplying by the density of liquid alumina. For the presented case, a mass of  $8.8 \cdot 10^{-12} \text{ kg}$  is computed for the cloud. The mass of the particle being of about  $2.9 \cdot 10^{-10} \text{ kg}$ , the mass of the cloud at a given instant represents about 3% of the mass of the particle. Upon partially integrating the profile, it is also measured that about 2.5% of the mass of the cloud is located within 1 and 1.5 particle radii.

<sup>2</sup> Basically, Navier-Stokes equations are solved around a burning droplet with an aluminum kinetic mechanism.

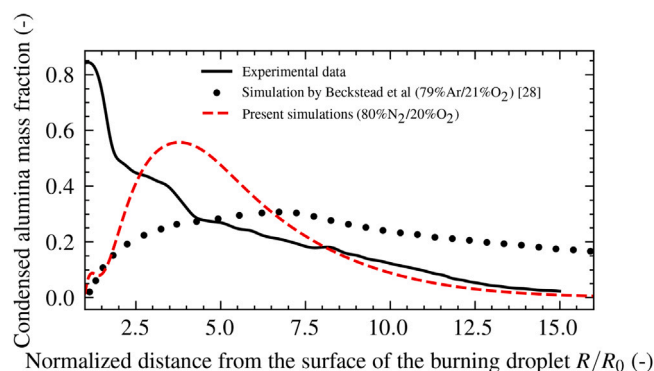


Fig. 15. Comparison of experimental mass fraction profile and simulated ones.

## 5. Conclusion

The paper introduces a multispectral application of the light extinction method, which enables the measurement of the size distribution profile of oxide particles. This is achieved by measuring the optical depths of the surrounding of the droplet at different wavelengths. Determining the size profile of particles forming the smoke enables the measurement of the volume fraction of oxide without relying on the Rayleigh approximation. An accurate concentration profile is thus obtained by the means of this non-intrusive method. Observations show that the radius of alumina particles in the cloud ranges from approximately 75 nm in the reaction zone to about 85 nm in the condensation zones. A volume fraction of  $2.8 \cdot 10^{-4}$  is observed near the particle surface compared to a value of about  $3 \cdot 10^{-5}$  further in the cloud. Both these obtained profiles provide new insights into the phenomenology of aluminum droplet combustion and offer new reference data for simulations. A comparison between the experimental data and simulation data from existing literature reveals important discrepancies between the observations and current models. The evaluation of the amount of alumina as well as its size and location will help in better simulating the single burning particle case as well as better assessing the potential collective interactions in aluminum dust flames. This paper serves as a reference case for the introduced method, with future work focusing on characterizing this oxide cloud in environments with varying compositions and pressures. Moreover, measuring an optical depth profile provides an absorbance profile for all the three wavelengths used in this study. Since local absorbance equates to local emissivity, and since local emission can be obtained through deconvolution of a flame emission image without backlight, it is possible through the ratio of local emission to local emissivity to measure a local blackbody emission. By using a blackbody calibration for the camera, a temperature profile of condensed oxides surrounding the droplet can be measured through a pyrometric method, using the ratio of two blackbody emission images. This single experiment would then allow to fully characterize the oxide smoke by obtaining size, temperature and concentration profiles, all spatially resolved, for any given time of the combustion observed by the camera.

## CRedit authorship contribution statement

**Hugo Keck:** Writing – review & editing, Writing – original draft, Methodology, Formal analysis. **Christian Chauveau:** Supervision, Conceptualization. **Guillaume Legros:** Supervision, Methodology. **Stany Gallier:** Supervision, Investigation. **Fabien Halter:** Supervision, Investigation.

## Declaration of competing interest

The authors declare that they have no known competing financial interests or personal relationships that could have appeared to influence the work reported in this paper.

## Acknowledgments

The authors express their gratitude to the French Defense Procurement Agency DGA (Direction Générale de l'Armement) for their financial support.

## References

- [1] V.N. Emelyanov, I.V. Teterina, K.N. Volkov, Dynamics and combustion of single aluminium agglomerate in solid propellant environment, *Acta Astronaut.* 176 (2020) 682–694.
- [2] X. Zou, N. Wang, L. Han, R. Xue, C. Xu, W. Zhuang, B. Shi, Investigation on burning behaviors of aluminum agglomerates in solid rocket motor with detailed combustion model, *Acta Astronaut.* 206 (2023) 243–256.
- [3] J.M. Bergthorson, S. Goroshin, M.J. Soo, P. Julien, J. Palecka, D.L. Frost, D.J. Jarvis, Direct combustion of recyclable metal fuels for zero-carbon heat and power, *Appl. Energy* 160 (2015) 368–382.
- [4] S. Goroshin, J. Palečka, J.M. Bergthorson, Some fundamental aspects of laminar flames in nonvolatile solid fuel suspensions, *Prog. Energy Combust. Sci.* 91 (2022) 100994.
- [5] M. Soo, X. Mi, S. Goroshin, A.J. Higgins, J.M. Bergthorson, Combustion of particles, agglomerates, and suspensions – A basic thermophysical analysis, *Combust. Flame* 192 (2018) 384–400.
- [6] V.A. Babuk, V.A. Vasilyev, Model of aluminum agglomerate evolution in combustion products of solid rocket propellant, *J. Propuls. Power* 18 (2002) 814–823.
- [7] M.K. King, Aluminum combustion in a solid rocket motor environment, *Proc. Combust. Inst.* 32 (2009) 2107–2114.
- [8] I. Glassman, R. Yetter, *Combustion*, Elsevier Inc., San Diego, USA, 2008.
- [9] V.E. Zarko, O.G. Glotov, Formation of Al oxide particles in combustion of aluminized condensed systems, *Sci. Technol. Energy Mater.* 74 (2013) 139–143.
- [10] S. Gallier, A. Braconnier, F. Godfroy, F. Halter, C. Chauveau, The role of thermophoresis on aluminum oxide lobe formation, *Combust. Flame* 228 (2021) 142–153.
- [11] M. Salita, Survey of recent Al<sub>2</sub>O<sub>3</sub> droplet size data in solid rocket chambers, nozzles, and plumes, in: *JANNAF Meeting*, Vol. 1, 1994, p. 1.
- [12] A. Genot, S. Gallier, T. Schuller, Thermo-acoustic instabilities driven by fuel droplet lifetime oscillations, *Proc. Combust. Inst.* 37 (2019) 5359–5366.
- [13] E.L. Dreizin, Experimental study of aluminum particle flame evolution in normal and micro-gravity, *Combust. Flame* 116 (1999) 323–333.
- [14] P. Bucher, L. Ernst, F. Dryer, R.A. Yetter, T.P. Parr, D.M. Hanson-Parr, Detailed studies on the flame structure of aluminium particle combustion, solid propellant chemistry, combustion, and motor interior ballistics, progress in astronautics and aeronautics, *AIAA J.* 185 (2000) 689–722.
- [15] J. Finke, F. Sewerin, A combined PBE-CFD approach for modelling the formation and dispersion of oxide smoke in homogeneous aluminum combustors and around a burning aluminum particle, in: *Proceedings of the European Combustion Meeting 2023*, 2023.
- [16] O. Orlandi, S. Gallier, Y. Moonsamy, N. Cesco, Numerical simulation of a single aluminum droplet burning in a propellant environment, in: *5th European Conference for Aeronautics and Space Sciences, EUCASS*, 2013.
- [17] A.Y. Lukin, A.M. Stepanov, Dispersion of the combustion products of metal particles, *Combust. Explos. Shock Waves* 19 (1983) 287–295.
- [18] V. Sarou-Kanian, Experimental Study of the Aluminum Droplet Combustion Under Forced Convection. Influence of the Gaseous Atmosphere (Ph.D. thesis), 2003.
- [19] T. Jenkins, R. Hanson, Soot pyrometry using modulated absorption/emission, *Combust. Flame* 126 (2001) 1669–1679.
- [20] G. Legros, Q. Wang, J. Bonnetty, M. Kashif, C. Morin, J.-L. Consalvi, F. Liu, Simultaneous soot temperature and volume fraction measurements in axis-symmetric flames by a two-dimensional modulated absorption/emission technique, *Combust. Flame* 162 (2015) 2705–2719.
- [21] J. Zhou, M. Zhou, L. Ma, Y. Wang, Planar light extinction measurement of soot volume fraction in laminar counterflow diffusion flames, *Front. Mech. Eng.* 7 (2021) 1–9.
- [22] R. Jalain, J. Bonnetty, A. Matynia, J.M. Citerne, H. Dutilleul, A. Jocher, J.L. Consalvi, G. Legros, Influence of sub-atmospheric pressure on flame shape and sooting propensity in ethylene laminar coflow non-premixed flame, *Combust. Flame* 259 (2024) 113173.
- [23] C.F. Bohren, D.R. Huffman, *Absorption and Scattering of Light by Small Particles*, WILEY-VCH Verlag GmbH & Co. KGaA, 1998.
- [24] L.A. Dombrovsky, Near-infrared properties of droplets of aluminum oxide melt, in: *Thermopedia*, Begel House Inc., ISBN: 1567004563, 2011.
- [25] V. Glasziou, Etudes Expérimentales des Mécanismes de Combustion de Particules D'aluminium en Milieux Gazeux Sous Pression (Ph.D. thesis), 2024.

- [26] K. McNesby, S. Dean, R. Benjamin, J. Grant, J. Anderson, J. Densmore, Imaging pyrometry for most color cameras using a triple pass filter, *Rev. Sci. Instrum.* 92 (2021) 063102.
- [27] O.G. Glotov, A.A. Onischuk, V.V. Karasev, V.E. Zarko, A.M. Baklanov, Size and morphology of the nanooxide aerosol generated by combustion of an aluminum droplet, *Dokl. Phys. Chem.* 413 (2007) 59–62.
- [28] I. González De Arrieta, C. Blanchard, P. Laboureur, C. Chauveau, C. Genevois, O. Rozenbaum, F. Halter, Radiative properties of micron-sized Al/Air premixed flames described by an effective medium core-shell formulation, *Int. J. Heat Mass Transf.* 203 (2023) 123815.
- [29] M.W. Beckstead, A summary of aluminum combustion, in: *RTO/VKI Special Course on “Internal Aerodynamics in Solid Rocket Propulsion”*, NATO, 2002.